Propulsion and Power Research

ORGINAL ARTICLE

Dynamic simulation and experimental validation of a two-phase closed thermosyphon for geothermal application

Johann-Christoph Ebeling[a,*], Xing Luo[a], Stephan Kabelac[a], Sebastian Luckmann[b], Horst Kruse[b]

[a]*Institute for Thermodynamics, Leibniz University of Hannover, Callinstraße 36, 30167 Hannover, Germany*
[b]*Forschungszentrum für Kältetechnik und Wärmepumpen GmbH, Weidendamm 14, 30167 Hannover, Germany*

Abstract   The heat transfer performance of a vertical two-phase closed thermosyphon (TPCT) used in a geothermal heat pump was experimentally investigated. The TPCT is a vertical plain steel pipe with inner diameter of 114 mm and bored 368 m deep underground. Carbon dioxide (CO_2) is used as working fluid. In the TPCT there is no condensation section. CO_2 is condensed by the evaporator of the heat pump, flows into the head of the TPCT and runs down as a falling film along the inner wall of the pipe. For the heat transfer simulation in the TPCT, a quasi-dynamic model in which the mass transfer between the liquid and vapor phases as well as the conduction heat transfer from the surrounding soil towards the pipe is treated dynamically. However the film flow modeling is based on the Nusselt theory of film condensation. The comparison of the experimental data with the numerical simulation is presented and discussed.

1. Introduction

Geothermal heat is an effective heat source for heat pumps used for space heating. Especially in winter heat pumps using geothermal heat by a two-phase closed thermosyphon (TPCT) are very reliable. Current geothermal thermosyphons have a length of 100 ∼ 150 m, which is

*Corresponding author. Tel.: (+49 511) 762 5659.

E-mail address: ebeling@ift.uni-hannover.de (Johann-Christoph Ebeling).

Nomenclature

C_f	Darcy friction factor
c_p	specific heat at constant pressure (unit: J/(kg · K))
D	inner diameter of the heat pipe (unit: m)
D_o	outer diameter of the heat pipe (unit: m)
g	gravitational acceleration (unit: m/s^2)
Gr	Grashof number
Δh_{fg}	evaporation enthalpy (unit: J/kg)
L	length of the heat pipe (unit: m)
m	fluid mass in a cell (unit: m)
m_{total}	total filling mass in the heat pipe (unit: kg)
$\dot{m}_{fg}$	mass transfer rate from liquid to vapor (unit: kg/s)
$\dot{m}_l$	liquid mass flow rate (downward) (unit: kg/s)
$\dot{m}_v$	vapor mass flow rate (upward) (unit: kg/s)
p	pressure (unit: Pa)
Pr	Prandtl number
$\dot{q}$	heat flux (unit: W/m^2)
r	radial coordinate (unit: m)
R	inner radius of the pipe (unit: m)
Re	Reynolds number
t	time (unit: s)
T	temperature (unit: K)
w_l	liquid velocity (downward) (unit: m/s)
$w_{l,\delta}$	liquid velocity at film/vapor interface (downward) (unit: m/s)
w_v	vapor velocity (upward) (unit: m/s)
y	coordinate perpendicular to the pipe wall (unit: m)
z	downward axial coordinate (unit: m)

Greek letters

|	
α	heat transfer coefficient (unit: W/(m^2 · K))
β	volumetric thermal expansion coefficient (unit: 1/K)
δ	thickness of falling liquid film (unit: m)
ε	void fraction
λ	thermal conductivity (unit: W/(m · K))
μ	dynamic viscosity (unit: Pa · s)
ρ	density (unit: kg/m^3)
τ	shear stress (unit: Pa)

Subscripts

cr	critical point
f	working fluid
fg	phase change from liquid to vapor
i	upper interface of a cell
$i+1$	lower interface of a cell
l	liquid
lam	laminar
m	mean value
pb	pool boiling
s	saturation
tur	turbulent
v	vapor
w	wall

sufficient to supply a heat pump for a single-family house [1]. However, these systems do not meet the needs of an urban heating system because their thermal power is low and the amount of sites for boreholes is limited in urban areas. Therefore, geothermal thermosyphons with higher thermal power for urban application are demanded.

A lot of research work has been done on the thermal performance of TPCTs for geothermal heat pumps. Dobran [2] presented an analytical model for determining the steady-state characteristics and stability thresholds of a TPCT. His analytical model was based on a lumped parameter description of the system that includes the thermohydraulics of vapor core, liquid film and liquid pool of the evaporator. Reed and Tien [3] presented a thermosyphon model consisting of the transient one-dimensional governing equations for mass, momentum and energy balances in the liquid film and vapor core coupled with the correlations for shear stress and heat transfer coefficients to predict the steady-state and transient performance of the TPCTs. Harley and Faghri [4] developed a transient two-dimensional model in which the vapor flow as well as the heat conduction in the pipe wall were treated as two-dimensional and were solved numerically with SIMPLE scheme. A quasi-steady Nusselt solution was used for modeling the liquid film. Pan [5] developed a condensation model for a TPCT by considering the interfacial shear due to mass transfer and interfacial velocity, which showed the

significance of the interfacial shear on the condensation inside the thermosyphon. Jiao et al. [6] conducted a set of experimental measurements and developed their theoretical model for condensation and film evaporation considering the interfacial shear stress between the liquid film and vapor flow in the Nusselt condensation theory. A drift flux model for void fraction was used for modeling the pool boiling. Shabgard et al. [7] developed a mathematical model for the transient performance of vertical thermosyphons. The flow and heat transfer in the vapor space were solved numerically by the use of a finite volume scheme. The condensate film was modeled using a quasi-steady Nusselt solution taking into account the effects of pressure gradient and interfacial shear stress. Recently, Xu et al. [8] developed a CFD model, which coupled the volume of fluid model, phase change model and continuum surface force model for a numerical simulation of heat transfer and fluid flow in a TPCT. By using transient mass transfer time relaxation parameters, their numerical results agree well with the experimental data. Jafari et al. [9] presented a review of experimental tests and applications, and summarized the correlations for calculation of condensation and evaporation in TPCTs. The experimental investigations were also performed on the vertical tubes with large diameter. Pashkevich and Muratov [10] performed the experiments on upward steam flow condensation inside a vertical duralumin tube with the internal diameter of 200 mm. It
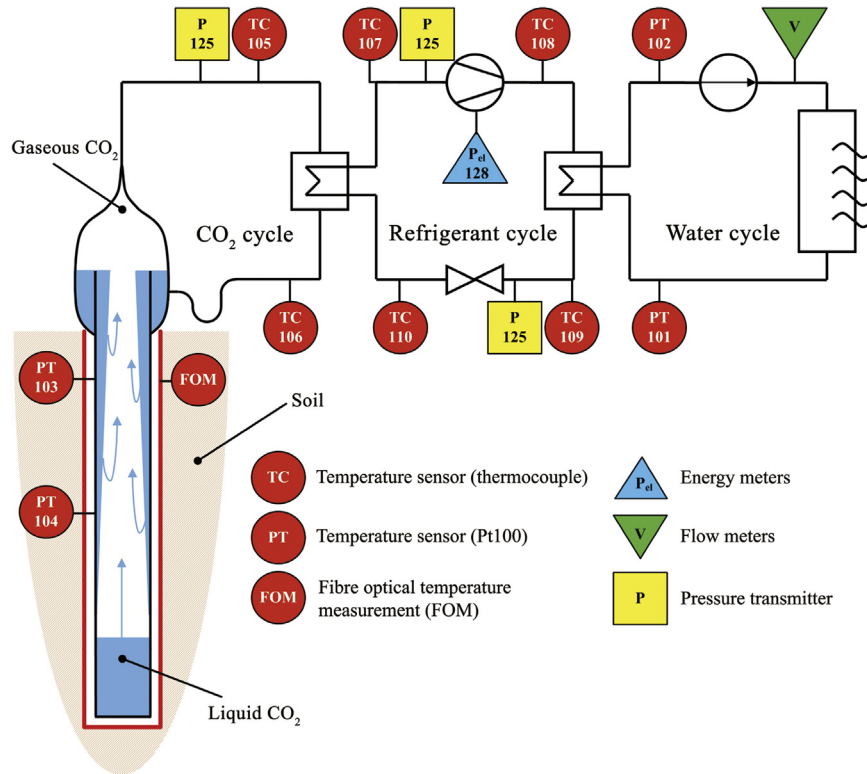
Figure 1 Schematic of the field test plant in operation.

is worth noting that their experimental data were much lower than the Nusselt solution, which might be due to non-uniform distribution of falling film.

Experimental investigations on TPCTs as a heat source for heat pumps with carbon dioxide have been carried out by Kruse [11]. Storch [12] made very detailed investigations on geothermal heat pipes using propane as a working fluid. A fundamental study on the heat transfer inside a thermosyphon and its thermal limits was given by Groß [13]. Ebeling et al. [14] reported their experimental results of two geothermal carbon dioxide heat pipes drilled about 400 m deep underground, which are compared to a simulation for the steady state. One is a plain steel pipe with an inner diameter of 114 mm and the other is a helically corrugated pipe with an inner diameter of 98 mm. Because carbon dioxide is a natural, non-flammable and environmentally friendly working fluid it can be installed in water protection areas. Due to its high liquid and vapor density at a working pressure of about 35–60 bar, pipes with low diameters can be used. Such a kind of the geothermal heat pipe is a TPCT, however the condensation takes place in the evaporator of the geothermal heat pump, and only the evaporation occurs in the vertical pipe in the liquid film/vapor region and pool region.

A sufficient simulation of the heat and mass transfer inside a geothermal heat pipe coupled to the surrounding soil is not published yet. A first simulation procedure for the investigation of the dynamic behavior of a plain steel heat pipe was developed and presented in Ref. [15] by Ebeling et al. This MATLAB code for modeling the transient heat transfer inside the pipe coupled with heat conduction in the pipe wall

and surrounding soil was further elaborated. In the present work, more experimental data is used for validation. Earlier simulations revealed that the modification of pool boiling heat transfer coefficient with the void fraction [6] would underestimate the pool boiling heat transfer. The Cooper correlation [16] could well predict the pool boiling in the TPCT with large inner diameter. The present work describes the current status of the model and simulation procedure. The model is validated with measured data taken from the field test rig installed in Nienburg/Weser (Germany), see Figure 1.

2. On-site experiments

A field test project with two CO_2-TPCTs within 50 m distance from each other is successfully in operation in Nienburg/Weser (Germany). The helically corrugated pipe was set up on site continuously from a coil in one piece, while the plain steel pipe had to be welded using pipes of 10 m length. The present work is focused on the plain pipe, which has a length $L = 368$ m, inner diameter $D = 114$ mm and outer diameter $D_o = 127$ mm, and is designed to collect about 22 kW of heat from the surrounding soil. Carbon dioxide (CO_2) is used as the working fluid of the TPCT. The total filling mass of CO_2 is 642 kg.

The TPCT is connected to a vapor-compression heat pump using the refrigerant R410A as working fluid. The compressor of the heat pump has an electrical consumption of about 7.5 kW. During the test runs, the evaporation temperature of the refrigerant was between $0 \sim 5\ °C$ with a
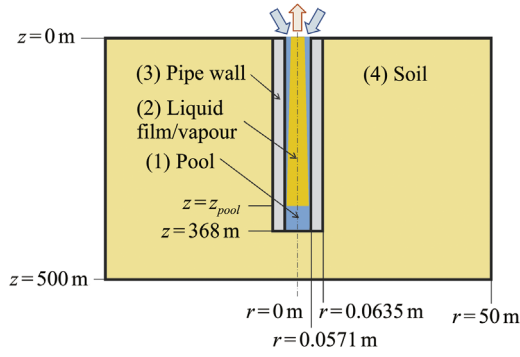
Figure 2 Calculation regions of the geothermal heat pipe.

heat load of about 25 kW. The refrigerant entering the condenser had an overheated temperature of 80–90 °C and was cooled in the condenser to the condensation temperature of 35 °C. Meanwhile, the water was heated in the condenser from 35 °C to 45 °C for space heating.

As is shown in Figure 1, the heat load needed for evaporating the refrigerant in the evaporator of the heat pump is supplied by condensating the gaseous CO_2 leaving the TPCT. The CO_2 vapor condenses inside a plate heat exchanger and the condensate (liquid CO_2) runs back to the TPCT and falls down along the inner wall of the pipe. While the liquid CO_2 flows down, it is heated by the surrounding soil through the pipe wall and evaporates. The rest of the liquid flow might reach the pool region where the liquid is further heated and boils. Due to the density difference the vapor rises up to the pipe head and is available for condensation by the evaporator of the heat pump. Figure 1 shows a schematic flowchart of the geothermal heat pump plant.

The test rig is equipped with resistive temperature sensors (PT), thermocouples (TC), pressure transducers (P), a flow meter (V) and an electric power meter (P_{el}) for the compressor motor, see Figure 1. The temperature distribution along the pipe wall is measured with a fiber optic temperature measurement technique (FOM). Therefore, a fiber optic cable used in communication technology is attached to the outside of the pipe. The two resistive temperature sensors attached to the outer pipe surface (PT103, PT104) are used for validating the data gathered by the FOM solely.

For modeling the transient heat transfer process of the TPCT, some measured test data are taken as the input data of the simulation, such as the pressure at the head of the TPCT, as well as the measured temperature variation of the pipe wall at the ground surface position ($z = 0$ m), which is taken as the boundary condition at $z = 0$ m and $0.0571 \text{ m} \leq r \leq 50 \text{ m}$, see Figure 2. More details about the experiments can be found in Ref. [14].

3. Theoretical model

The heat transfer process for the geothermal thermosyphon consists of four parts: (1) boiling or convective heat transfer in the pool region, (2) evaporation/condensation or vapor convective heat transfer in the liquid film/vapor region, (3) heat conduction in the pipe wall, (4) heat conduction in the surrounding soil region. The four corresponding calculation regions are shown in Figure 2. The whole region is divided into 500 subsections in the vertical direction (denoted by index i). In the radial direction, the fluid and pipe wall occupy one subsection for each, and the soil region is divided into 48 subsections (denoted by index j). Totally there are 25,000 cells.

3.1. Conservation of mass

For convenience we define that the vapor flow direction is upward, and the liquid flow direction is downward. In each cell the conservation equation of mass for the vapor phase and liquid phase can be written as.

$$\frac{dm_v}{dt} = \dot{m}_{fg} + \dot{m}_{v,i+1} - \dot{m}_{v,i} \tag{1}$$

$$\frac{dm_l}{dt} = \dot{m}_{l,i} - \dot{m}_{l,i+1} - \dot{m}_{fg} \tag{2}$$

where m_v and m_l are the mass of vapor and liquid per cell, $\dot{m}_{v,i+1}$ and $\dot{m}_{l,i}$ are the mass flow rates of the vapor and liquid entering the cell, $\dot{m}_{v,i}$ and $\dot{m}_{l,i+1}$ are those leaving the cell. Following from:

$$\dot{Q} = \dot{m}_{fg} \cdot \Delta h_{fg} = \dot{q} \cdot A \tag{3}$$

the mass transfer rate from the liquid phase to the vapor phase, $\dot{m}_{fg}$, can be calculated by Eq. (4) if there is a phase change (evaporation or condensation),

$$\dot{m}_{fg} = \frac{\dot{q} \pi D \Delta z}{\Delta h_{fg}} \tag{4}$$

where Δh_{fg} is the evaporation enthalpy, D is the inner diameter of the pipe, and $\dot{q}$ is the heat flux,

$$\dot{q} = \alpha (T_w - T_f) \tag{5}$$

Eqs. (1) and (2) are applied to all cells inside the pipe. The transient terms at the left side of the equations can be discretized with an implicit scheme,

$$\frac{dm}{dt} \approx \frac{m - m^{(0)}}{\Delta t} \tag{6}$$

where m can be either m_l or m_v and "(0)" denotes its value at the last time level.

3.2. Model for pool region

In the pool region, whether the boiling would happen depends on the excess temperature $\Delta T_e = T_w - T_s$. For simplicity we assume a zero excess temperature $\Delta T_e = 0$, that means, if the wall temperature T_w is higher than the saturation temperature T_s, pool boiling occurs, otherwise

there is only a natural convection heat transfer. The calculation consequence in the pool region is upward, beginning from the pipe bottom with the bottom cell of the pipe. The heat transfer coefficient for the bottom surface of the pipe is calculated according to the correlations [17,18],

$$\alpha_{natural,bottom} = \frac{\lambda_{l,m}}{R} \times C(GrPr)_l^{1/6} \qquad (7)$$

in which $C = 1.076$ for heating and $C = 0.747$ for cooling.

For the natural convection heat transfer inside a vertical cylinder we use the equation of Elenbaas [19] and rewrite it for each cell in the pool region as

$$\alpha_{natural,l} = \frac{\lambda_{l,m}(GrPr)_l}{16(z_{i+1}-z_i)} \left\{ \exp\left[-16 \left(\frac{0.5(L-z_{i+1})}{R(GrPr)_l} \right)^{3/4} \right] \right. $$
$$\left. - \exp\left[-16 \left(\frac{0.5(L-z_i)}{R(GrPr)_l} \right)^{3/4} \right] \right\} \qquad (8)$$

where

$$(GrPr)_l = \frac{\rho_{l,m}^2 c_{p,l,m} g \beta_{l,m} R^3 \Delta T}{\mu_{l,m} \lambda_{l,m}}. \qquad (9)$$

If the wall temperature is lower than or equal to the saturation temperature, no boiling occurs. In this case the liquid temperature should be calculated with the energy equation for single phase pipe flow. We formulate the convective heat transfer in the energy equation for the pool region with an upwind scheme,

$$\frac{d}{dt}(c_{p,m} m_l T_{f,i}) + [\max(-\dot{m}_{l,i},0) + \max(\dot{m}_{l,i+1},0)]c_{p,m}T_{f,i}$$
$$= c_{p,m}[\max(\dot{m}_{l,i},0)T_{f,i-1} - \max(-\dot{m}_{l,i+1},0)T_{f,i+1}$$
$$+ \alpha\pi D\Delta z(T_{w,i} - T_{f,i}). \qquad (10)$$

According to the assumption of a zero excess temperature, pool boiling occurs if the wall temperature is higher than the saturation temperature. In such a case the fluid temperature remains at the saturation temperature and the Cooper correlation [16] can be used for calculating the heat transfer coefficient,

$$\alpha_{pb} = 55\dot{q}^{0.67}M^{-0.5}(p/p_{cr})^{(0.12-0.2\lg(R_p))}(-\lg(p/p_{cr}))^{-0.55} \qquad (11)$$

in which the units of α_{pb} and $\dot{q}$ are W/(m$^2 \cdot$ K) and W/m^2, respectively. M is the molar mass of CO_2, $M = 44.01$ kg/kmol, p_{cr} is the critical pressure of CO_2, $p_{cr} = 73.773$ bar, and the surface roughness $R_p = 0.4$ μm.

In the pool region, the mass of vapor or liquid in a cell is given by Eqs. (12) and (13),

$$m_v = \varepsilon\rho_v \frac{\pi}{4}D^2\Delta z \qquad (12)$$

$$m_l = (1-\varepsilon)\rho_l \frac{\pi}{4}D^2\Delta z. \qquad (13)$$

The void fraction ε in Eq. (13) is calculated with the drift flux model of Kataoka and Ishii [20],

$$\varepsilon = \frac{j_v}{C_0 j_v + V_{vj}}, \qquad (14)$$

in which the superficial velocity of gas and liquid in Eq. (14) are defined as $j_v = 4\dot{m}_v/(\rho_v\pi D^2)$, and V_{vj} is the drift velocity, $V_{vj} = V_{vj}^+\left(\sigma g(\rho_l-\rho_v)^{1/2}/\rho_l\right)^{1/2}$. C_0 is a distribution parameter. For a round tube, $C_0 = 1.2 - 0.2\sqrt{\rho_v/\rho_l}$. The dimensionless drift velocity V_{vj}^+ can be calculated with the correlation [20]:

$$V_{vj}^+ = 0.0019\overline{D}^*(\rho_l/\rho_v)^{0.157}\overline{N}_\mu^{-0.562} \qquad (15)$$

$$\overline{D}^* = \min\left\{ D/\sqrt{\frac{\sigma}{g(\rho_l-\rho_v)}},\ 30 \right\} \qquad (16)$$

$$\overline{N}_\mu = \min\left\{ \mu_l \left(\rho_l\sigma\sqrt{\frac{\sigma}{g(\rho_l-\rho_v)}} \right)^{-1/2},\ 2.25 \times 10^{-3} \right\}. \qquad (17)$$

With known heat transfer coefficient and the vapor mass flow rate entering the cell ($\dot{m}_{v,i+1}$), the vapor mass flow rate leaving the cell ($\dot{m}_{v,i}$) can be obtained with Eq. (1) and other related equations. In the same way, the liquid flow rate entering the cell ($\dot{m}_{l,i}$) is determined by Eq. (2) with known $\dot{m}_{l,i+1}$.

3.3. Model for liquid film/vapor region

In the liquid film/vapor region different forms of heat transfer can occur along the pipe, mainly evaporation, condensation or single phase convective heat transfer (vapor). The cells in this region can be treated as wet cells (two-phase) and dry cells (single phase).

3.3.1. Wet cell
If a liquid film exists, the vapor in a cell is saturated. Whether an evaporation or condensation occurs depends on whether the wall temperature is higher than the saturation temperature. In both cases the heat transfer coefficient is dominated by the thickness of the liquid film. In the present work, the quasi-steady Nusselt-type solution procedure used by Refs. [4–7] is adopted for modeling the falling film. In this procedure the following assumptions are made: (1) The transient term and fluid inertia in the momentum equation is neglected. (2) The velocity component in horizontal direction is neglected. (3) The liquid film thickness is much smaller than the vapor space radius. Based on these assumptions, the momentum equation for the liquid film is simplified to

$$\frac{d^2 w_l}{dy^2} = -\frac{(\rho_l-\rho_v)g}{\mu_l} \qquad (18)$$

$$y = 0: \quad w_l = 0; \qquad y = \delta: \quad \frac{dw_l}{dy} = -\frac{\tau_\delta}{\mu_l} \tag{19}$$

in which τ_δ is the interfacial shear stress between the liquid film and vapor flow,

$$\tau_\delta = \frac{C_f}{4}\frac{\rho_v}{2}(w_{l,\delta} + w_v)^2 - \frac{\dot{m}_{fg}}{\pi D \Delta z}(w_{l,\delta} + w_v) \tag{20}$$

As has been mentioned afore, the velocity direction of the liquid (w_l) is downward, and that of the vapor flow (w_v) is upward. Integrating Eq. (18) twice with respect to y using the boundary condition (19), we obtain the liquid mass flow rate and velocity at the interface as follows, respectively,

$$\dot{m}_l = \frac{\pi D \rho_l \delta^2}{\mu_l}[g(\rho_l - \rho_v)\delta/3 - \tau_\delta/2] \tag{21}$$

$$w_{l,\delta} = \frac{\delta}{\mu_l}\left[g(\rho_l - \rho_v)\delta/2 - \tau_\delta\right]. \tag{22}$$

With given liquid mass flow rate $\dot{m}_l$, the film thickness δ can be obtained by solving Eq. (21).

The correlations of Darcy friction factor appearing in Eq. (20) are taken from the literature for different Reynolds numbers:

Laminar flow:

$$C_f = 64/Re_v$$
$$(Re_v \le 2000) \tag{23a}$$

Blasius:

$$C_f = 0.3164 Re_v^{-0.25}$$
$$(3000 < Re_v \le 10^5) \tag{23b}$$

Hermann:

$$C_f = 0.0054 + 0.3964 Re_v^{-0.3}$$
$$(2 \times 10^4 < Re_v \le 5 \times 10^7) \tag{23c}$$

Gnielinski:

$$C_f = \left[1.819 \log_{10}(Re_v) - 1.64\right]^{-2}$$
$$(10^6 < Re_v \le 5 \times 10^7) \tag{23d}$$

Prandtl-Karman:

$$C_f = \left[2 \log_{10}\left(\sqrt{C_f} Re_v\right)\right]^{-2}$$
$$(2 \times 10^6 < Re_v) \tag{23e}$$

For the transition region $2000 < Re_v \le 3000$, an interpolation between Eqs. (23a) and (23b) is used. The Reynolds number for the vapor flow is calculated as:

$$Re_v = \frac{4\dot{m}_v}{\mu_v \pi D}. \tag{24}$$

The heat transfer coefficient for falling film evaporation and condensation are based on the following Eq. [21]:

$$\alpha_{lam} = \left(\frac{\rho_l^2 g \lambda_l^3 \pi D}{3\mu_l \dot{m}_l}\right)^{1/3} = \left(\frac{4}{3}\right)^{1/3}\left(\frac{\rho_l^2 g \lambda_l^3}{\mu_l^2}\right)^{1/3} Re_{film}^{-1/3} \tag{25}$$

$$\alpha_{wave-lam} = 0.606\left(\frac{\rho_l^2 g \lambda_l^3}{\mu_l^2}\right)^{1/3}\left(\frac{Re_{film}}{4}\right)^{-0.22} \tag{26}$$

$$\alpha_{tur} = 3.8 \times 10^{-3}\left(\frac{\rho_l^2 g \lambda_l^3}{\mu_l^2}\right)^{1/3} Re_{film}^{0.4} Pr_l^{0.65} \tag{27}$$

in which the film Reynolds number is calculated as:

$$Re_{film} = \frac{4\dot{m}_l}{\mu_l \pi D}. \tag{28}$$

We have to enhance the ratio of heat transfer coefficient due to capillary waves on the film surface and turbulent flow,

$$C_{wave} = \frac{\alpha_{wave-lam}}{\alpha_{lam}} = 0.74693 Re_{film}^{1/3 - 0.22} \tag{29}$$

$$C_{tur} = \frac{\alpha_{tur}}{\alpha_{wave-lam}} = 4.6223$$
$$\times 10^{-3} Re_{film}^{0.62}\left(\frac{c_{p,l,m}\mu_{l,m}}{\lambda_{l,m}}\right)^{0.65} \tag{30}$$

which yields,

$$\alpha_{film} = C_{wave} C_{tur} \lambda_l / \delta. \tag{31}$$

The calculation consequence in the liquid film/vapor region is downward, beginning from the top end of the pipe. For each cell in this region, Eq. (2) is used to determine the liquid mass flow rate leaving the cell and entering the next cell,

$$\dot{m}_{l,i+1} = \dot{m}_{l,i} - \dot{m}_{fg} - \frac{dm_l}{dt} \tag{32}$$

in which $\dot{m}_{fg}$ is calculated with Eqs. (4), (5) and (31).

At the pipe inlet (the top end of the pipe) the liquid mass flow rate entering the first cell is at first assumed and then modified according to the calculated total filling mass of CO_2 in the TPCT,

$$\dot{m}_{l,1} = \dot{m}_{v,1} + \frac{m_{total} - m_{total}^*}{\Delta t},$$
$$m_{total}^* = \sum_{i=1}^{nz}(m_{l,i} + m_{v,i}) \tag{33}$$

where nz is the number of cells in the fluid. For each time step the inlet liquid mass flow rate is adjusted until the deviation between m_{total}^* and m_{total} is small enough.

3.3.2. Dry cell

For a dry cell, if the wall temperature is lower than the saturation temperature, the vapor will condense on the wall surface. We use the classical Nusselt solution presented in Harley [4] to estimate an initial value of the mean film thickness of the cell,

$$\delta = \frac{1}{2}\left[\frac{4\mu_l \lambda_l (T_s - T_w)\Delta z}{g\rho_l^2 \Delta h_{fg}}\right]^{1/4} \tag{34}$$

and then treat the cell as a wet one.

For the case of single phase convective heat transfer (the wall temperature is higher than the saturation temperature), the Gnielinski correlation [22] is used,

$$\alpha_{forced,v} = \frac{\lambda_v}{D} \frac{(f/8)(Re_v - 1000)Pr_v}{1 + 12.7\sqrt{f/8}(Pr_v^{2/3} - 1)} \quad (35)$$

for a forced convection heat transfer, in which

$$f = [1.82 \log_{10}(Re_v) - 1.64]^{-2}. \quad (36)$$

The Reynolds number for vapor flow Re_v from Eq. (25) is used.

The equation of Elenbaas [19] for natural convection heat transfer is expressed as

$$\alpha_{natural,v} = \frac{\lambda_v (GrPr)_v}{16\Delta z} \left\{ \exp\left[-16\left(\frac{0.5(z_{pool} - z_{i+1})}{R(GrPr)_v} \right)^{3/4} \right] \right. $$
$$\left. - \exp\left[-16\left(\frac{0.5(z_{pool} - z_i)}{R(GrPr)_v} \right)^{3/4} \right] \right\}. \quad (37)$$

The larger one between $\alpha_{forced,v}$ and $\alpha_{natural,v}$ will be used. The vapor temperature is calculated with the upwind scheme similar to Eq. (10).

3.4. Model for pool level

The cell containing the pool interface is denoted by the index i_{pool} ($z_{i_{pool}} \leq z_{pool} \leq z_{i_{pool}+1}$). This cell is divided into two parts: pool sub-cell ($z_{pool} \leq z \leq z_{i_{pool}+1}$) and liquid film/vapor-sub-cell ($z_{i_{pool}} \leq z < z_{pool}$). The calculation methods have been discussed afore. However, in this cell the liquid mass flow rates entering and leaving the cell are determined by the calculation for its upper and lower adjacent cells. Applying Eq. (2) approached with the implicit scheme of Eq. (6) to this interfacial cell would yield

$$m_l = m_l^{(0)} + (\dot{m}_{l,i} - \dot{m}_{l,i+1} - \dot{m}_{fg})\Delta t. \quad (38)$$

The new pool level can be evaluated by

$$z_{pool} = z_{i_{pool}+1} - \frac{m_l}{m_{l,\,max}}\Delta z \quad (39)$$

in which

$$m_{l,\,max} = (1 - \varepsilon)\rho_l \frac{\pi}{4}D^2\Delta z. \quad (40)$$

Obviously, the negative value of m_l indicates that the pool level should fall into the lower cell. If the calculated value of m_l is larger than its maximal value, $m_{l,max}$, the pool level should rise into the upper cell.

3.5. Model for pressure distribution

The pressure drop of vapor flow consists of frictional pressure drop Δp_f, static pressure drop Δp_g and pressure drop due to acceleration Δp_a,

$$\Delta p = \Delta p_f + \Delta p_g + \Delta p_a. \quad (41)$$

In the liquid film/vapor region the pressure drop is determined according to the vapor flow,

$$\Delta p_f = \frac{C_f \Delta z}{D - 2\delta} \frac{\rho_v}{2}(w_{l,\delta} + w_v)^2, \quad (42)$$

$$\Delta p_g = \frac{4}{\pi D^2} g m_v, \quad (43)$$

$$\Delta p_a = \frac{4}{\pi D^2}(\dot{m}_{v,i}w_{v,i} - \dot{m}_{v,i+1}w_{v,i+1}). \quad (44)$$

In the pool region the relative velocity between the two phases is low. Therefore the frictional pressure drop in the pool can be neglected. The static pressure drop and pressure drop due to acceleration are evaluated with Eqs. (45) and (42), respectively,

$$\Delta p_g = \frac{4}{\pi D^2} g(m_l + m_v) \quad (45)$$

$$\Delta p_a = \frac{4}{\pi D^2}(\dot{m}_{v,i}w_{v,i} - \dot{m}_{v,i+1}w_{v,i+1}$$
$$+ \dot{m}_{l,i}w_{l,i} - \dot{m}_{l,i+1}w_{l,i+1}). \quad (46)$$

we take the measured pressure as the inlet pressure p_1 and calculate the pressure distribution beginning from the pipe inlet,

$$p_{i+1} = p_i + \Delta p_i \quad (i = 1, 2, \cdots, nz). \quad (47)$$

3.6. Model for heat conduction in pipe wall and soil

A transient two-dimensional energy equation is applied to the coupled heat conduction in the pipe wall and surrounding soil region.

$$\rho c_p \frac{\partial T}{\partial t} = \frac{1}{r}\frac{\partial}{\partial r}\left(\lambda r \frac{\partial T}{\partial r}\right) + \frac{\partial}{\partial z}\left(\lambda \frac{\partial T}{\partial z}\right). \quad (48)$$

The temperature distribution at the boundary far away from the TPCT is taken from earlier measurements, when the geothermal heat pipe had not been filled with CO_2.

$$r = 50 \text{ m}: \ T_{soil}(z, 50, t) = T_{soil,\infty}(z). \quad (49)$$

This temperature distribution is also used as the initial temperature,

$$t = 0 \text{ s}: \ T_{soil}(z, r, 0) = T_{soil,\infty}(z). \quad (50)$$

The measured temperature variation of the pipe wall at the ground surface position is taken as the surface temperature of the whole calculation region

$$z = 0 \text{ m}: \ T_{soil}(0, r, t) = T_w(0, t). \quad (51)$$

At the bottom boundary of the soil region, we simply set an adiabatic boundary condition as

$$z = 500 \text{ m}: \ \frac{\partial T_{soil}}{\partial z} = 0. \quad (52)$$

At the interfaces between the fluid and inner wall of the pipe, the boundary conditions are expressed with

Test on 08-May-2015 (09:31:28–15:49:58)

Test on 04-Jun-2015 (10:47:21–16:38:21)
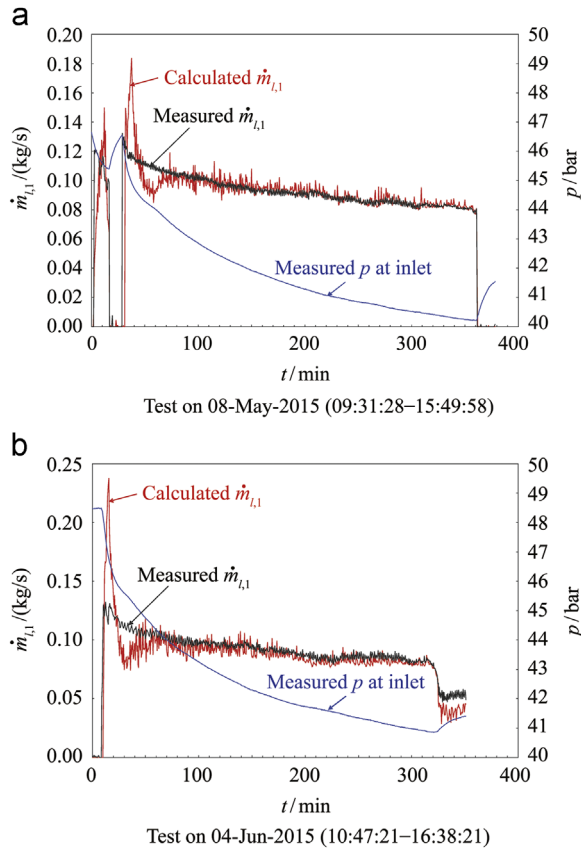
Figure 3   Measured pressure (p_1) and liquid mass flow rate ($\dot{m}_{l,1}$) at the pipe inlet and simulated liquid mass flow rate.

Test on 08-May-2015 (09:31:28–15:49:58)

Test on 04-Jun-2015 (10:47:21–16:38:21)

Figure 4   Measured and simulated wall temperatures (T_w) and simulated fluid temperature (T_f) at different pipe depths.

$$r = 0.0571 \text{ m}: \ \lambda_w \frac{\partial T_W}{\partial r} = \alpha(T - T_f), \tag{53}$$

$$z = 368 \text{ m}: \ \lambda_w \frac{\partial T_W}{\partial z} = \alpha(T - T_f). \tag{54}$$

The boundary conditions at the interfaces between the outer wall of the pipe and the soil are given for the pipe wall region and surrounding soil region.

Pipe wall region:

$$r = 0.0635 \text{ m}: \ \lambda_w \frac{\partial T_W}{\partial r} = \lambda_{soil} \frac{\partial T_{soil}}{\partial r}, \tag{55}$$

$$z = 374.43 \text{ m}: \ \lambda_w \frac{\partial T_W}{\partial z} = \lambda_{soil} \frac{\partial T_{soil}}{\partial z}. \tag{56}$$
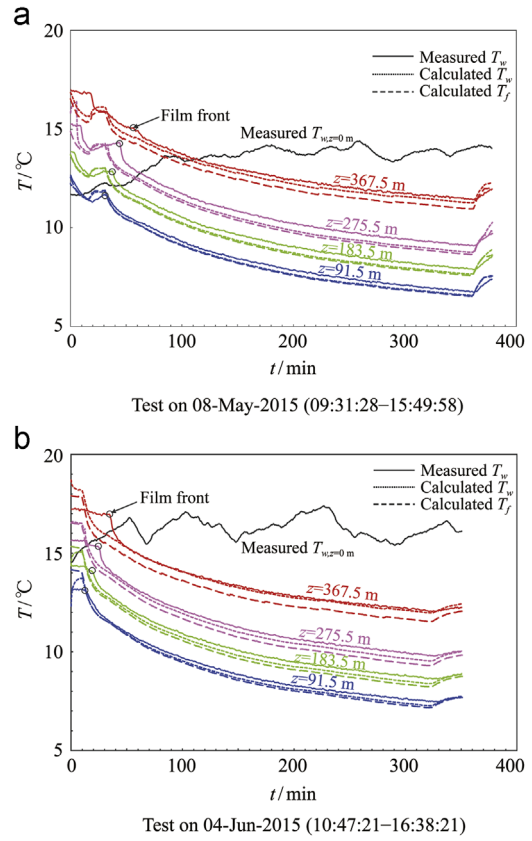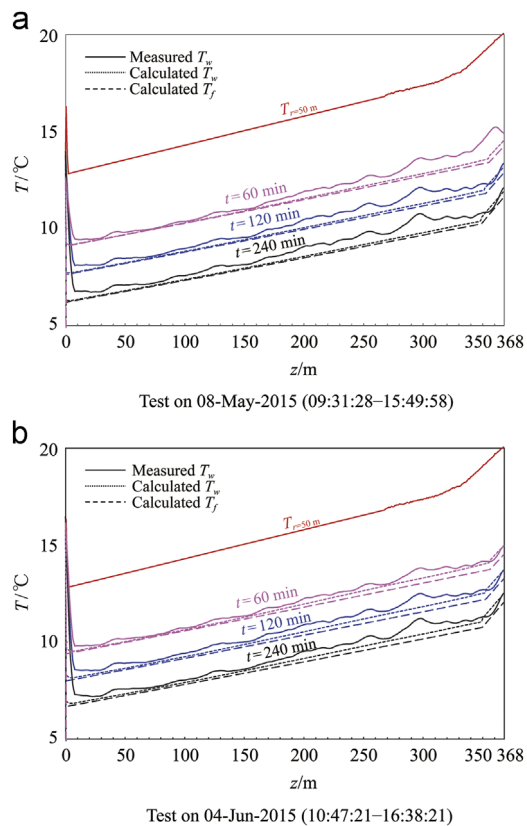
Soil region:

$$r = 0.0635 \text{ m}: \ T_{soil} = T_w, \tag{57}$$

$$z = 374.43 \text{ m}: \ T_{soil} = T_w. \tag{58}$$

The properties of the pipe and the soil used in the simulation are as follows:

$\lambda_w = 40 \text{ W/(m} \cdot \text{K)}, \rho_w = 7800 \text{ kg/m}^3, c_{p,w} = 470 \text{ J/(kg} \cdot \text{K)}.$ $\lambda_{soil} = 1.2 \text{ W/(m} \cdot \text{K)}, \rho_{soil} = 2285 \text{ kg/m}^3, c_{p,soil} = 1480 \text{ J/(kg} \cdot \text{K)}.$
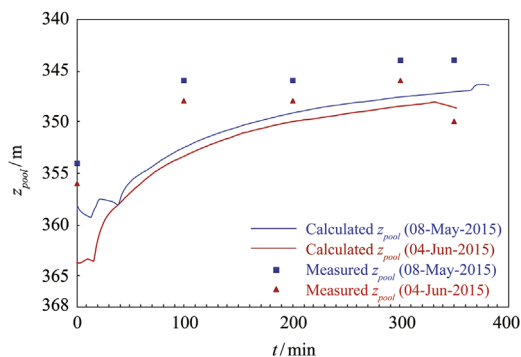
4. Results and discussions

Two sets of the experimental data to be investigated were taken from the on-site experiment in May and June 2015, respectively. The measurement started before the heat pump was turned on and ended after the heat pump was turned off. Therefore, the start-up and shutdown periods are included. The measured data and simulated results during the whole test period of the first test are shown in Figures 3(a)–5(a), and those of the second test are given in Figures 3(b)–5(b). In the first test, the heat pump was shortly turned off after the start-up and then turned on again. Figure 3(a) shows the corresponding liquid flow rate and pressure of CO_2 at the pipe inlet. In the simulation the measured inlet pressure and the wall temperature at ground surface ($z = 0$ m) are taken as input boundary conditions for the simulation.

Figure 3 shows a good agreement between the measured inlet liquid mass flow rate and its predicted value except in the start-up period, where a large deviation appears. Due to the lack of CO_2 and R410A flow meters, the mass flow rate of the condensed CO_2 at the inlet of the pipe is indirectly evaluated using the heat load of the water cycle. The dynamics of the heat pump have not yet been considered in the present simulation. Additionally the temperature distribution inside the soil is considered to be given by the temperature distribution taken before the pipe was filled

Figure 5 Measured and simulated wall temperatures (T_w) and simulated fluid temperature (T_f) along the pipe.

Figure 6 Measured and simulated development of the pool surface (z_{pool}).

propagation of the film line does not match the one obtained by the measurements, which are presented in Ref. [14]. The temperature profiles at $t = 60$ min, 120 min and 240 min are shown in Figure 5. The measured profile of the wall temperature taken by FOM is a little higher than the simulated one. This might be due to the contact heat resistance between the pipe wall and the temperature sensor. The deviation between the measured wall temperature and simulated results also occur in the start-up period, which might be caused by the assumption of the zero excess temperature used in the present simulation and should be further modified.

Figure 6 shows the development of the pool surface inside the geothermal heat pipe. The simulated results are compared to the measured pool surface, which is obtained by interpreting the change of the temperature profile taken by the FOM [14]. The simulated results are in very good correspondence with the measured ones. The difference of the simulated and measured pool surface averages to 4 m. From both data it can be seen that the pool surface rises during operation. This is on the one hand due to nucleate boiling inside the pool. On the other hand, the total mass of vapor inside the heat pipe declines with decreasing vapor density. Thus the liquid mass of CO_2 inside the pipe has to rise. Due to the low filling level of the heat pipe the detection of the pool surface by FOM is not always very accurate. For the purpose of a better validation of the simulation the filling level of the TPCT will be increased.

5. Conclusions

A dynamic simulation model for predicting the heat transfer performance of a vertical TPCT used in a geothermal heat pump was developed. Unlike common TPCTs, the geothermal thermosyphon has no condensation section in the pipe region. The working fluid is condensed inside the evaporator of a geothermal heat pump.

To validate the results of the dynamic simulation two sets of measurement data are used. The developed model shows good agreement with the measured data for long term operation. However, the phenomena during the start-up process are not represented very precisely yet. Nevertheless some interesting phenomena can be seen. (1) In the start-up period the soil temperature might be lower than the saturation temperature of the fluid, therefore, condensation especially in the upper regions of the pipe might occur, rather than evaporation. (2) Because of low heat conductivity of the soil, the heat transfer of the whole process is dominated by the heat conduction through the soil. It might be meaningful to carry out more tests to predict the initial soil temperature distribution and to evaluate the effective heat conductivity of the soil. (3) Because of a high vapor density of the CO_2, the vapor Reynolds number could be very high, and the vapor flow would be fully turbulent. The correlations used in the model should cover the high Reynolds number range. (4) The development of the pool

with CO_2. This assumption leads to a non-existing temperature gradient in radial direction. Thus the effect the heat pipe has on the temperature distribution inside the soil due to heat transfer in axial and radial direction is neglected. This might be the reason for the deviation between the measured and simulated mass flow during the start-up period. Further experimental work to investigate the dynamic behavior of the heat pump and the initial temperature distribution in the soil region will be carried out.

The progression of wall temperature at four different depths during the whole test are shown in Figure 4. From the measured data, one can see the propagation of the film front during the start-up period indicated by a sudden drop in the local wall temperature. So far the simulated

surface due to nucleate boiling inside the pool and the change in vapor density can be predicted reliably.

Until now we have not checked other correlations, i.e. those listed in Ref. [9] and other literature. A further investigation on the modeling of heat transfer performance of the geothermal thermosyphon based on more experimental data is demanded.

Acknowledgements

References

[1] A. Peterlunger, M. Ehrbar, S. Bassetti, E. Rohner, Pumpenlose Erdwärmesonde, Phase 1: Potentialabklärung, Machbarkeitsstudie energetisch und wirtschaftlich, Nov, 2004.

[2] F. Dobran, Steady-state characteristics and stability thresholds of a closed two-phase thermosyphon, Int. J. Heat. Mass Transf. 28 (1985) 947–957.

[3] J.G. Reed, C.L. Tien, Modeling of the two-phase closed thermosyphon, J. Heat. Transf. 109 (1987) 722–730.

[4] C. Harley, A. Faghri, Complete transient two-dimensional analysis of two-phase closed thermosyphons including the falling condensate film, J. Heat. Transf. 116 (1994) 418–426.

[5] Y. Pan, Condensation heat transfer characteristics and concept of sub-flooding limit in a two-phase closed thermosyphon, Int. Commun. Heat. Mass Transf. 28 (2001) 311–322.

[6] B. Jiao, L.M. Qiu, X.B. Zhang, Y. Zhang, Investigation on the effect of filling ratio on the steady-state heat transfer performance of a vertical two-phase closed thermosyphon, Appl. Therm. Eng. 28 (2008) 1417–1426.

[7] H. Shabgard, B. Xiao, A. Faghri, R. Gupta, W. Weissman, Thermal characteristics of a closed thermosyphon under various filling conditions, Int. J. Heat. Mass Transf. 70 (2014) 91–102.

[8] Z. Xu, Y.N. Zhang, B.X. Li, J.Q. Huang, Modeling the phase change process for a two-phase closed thermosyphon by considering transient mass transfer time relaxation parameter, Int, J. Heat. Mass Transf. 101 (2016) 614–619.

[9] D. Jafari, A. Franco, S. Filippeschi, P.D. Marco, Two-phase closed thermosyphons: a review of studies and solar applications, Renew. Sust. Energ. Rev. 53 (2016) 575–593.

[10] R.I. Pashkevich, P.V. Muratov, Film condensation in a large diameter tube with upward steam flow, Int. J. Heat. Mass Transf. 81 (2015) 804–810.

[11] H. Kruse, H. Rüssmann, S. Glawon, Oberflächennahe und mitteltiefe Oberflächennahe und mitteltiefe CO_2-Erdwärmerohre für Wärmepumpen höherer Leistung: Teilprojekt A: Oberflächennahes Erdwärmerohr, Hannover, May, 2015.

[12] T. Storch, Grundlegende Untersuchungen zum Wirkprinzip von geothermischen Phasenwechselsonden, Sierke Verlag, Göttingen, 2015.

[13] U. Groß, Kondensation und Verdampfung im geschlossenen Thermosyphon, VDI Verlag, Düsseldorf, 1991.

[14] J.-C. Ebeling, S. Kabelac, S. Luckmann, H. Kruse, Simulation and experimental validation of a 400 m vertical CO_2 heat pipe for geothermal application, in: Proceedings of Joint 18th IHPC and 12th IHPS, Jeju, Korea, June 12-16, 2016.

[15] J.-C. Ebeling, X. Luo, S. Kabelac, S. Luckmann, H. Kruse, Quasi-dynamic model for simulation of a 400 m vertical CO_2 heat pipe for geothermal application, in: Proceedings of the 9th International Symposium on Heat Transfer (ISHT9-Q0358), Beijing, China, Aug. 15-19, 2016.

[16] M.G. Cooper, Heat flows rates in saturated nucleate pool boiling - A wide-ranging examination using reduced properties, in: J.P. Hartnett, T.F. Irvine Jr. (Eds.), Advances in Heat Transfer, 16, Academic Press, Orlando, 1984, pp. 157–239.

[17] E.M. Sparrow, C.K. Carlson, Local and average natural convection Nusselt numbers for a uniformly heated, shrouded or unshrouded horizontal plate, Int. J. Heat. Mass Transf. 29 (3) (1986) 369–379.

[18] B. Chambers, T.Y.T. Lee, A Numerical study of local and average natural convection Nusselt numbers for simultaneous convection above and below a uniformly heated horizontal thin plate, J. Heat. Transf. 119 (1) (1997) 102–108.

[19] W. Elenbaas, The dissipation of heat by free convection the inner surface of vertical tubes of different shapes of cross-section, Physica 9 (8) (1942) 865–874.

[20] K. Isao, I. Mamoru, Drift flux model for large diameter pipe and new correlation for pool void fraction, Int. J. Heat. Mass Transf. 30 (9) (1987) 1927–1939.

[21] K.R. Chun, R.A. Seban, Heat transfer to evaporating liquid films, J. Heat. Transf. 93 (4) (1971) 391–396.

[22] V. Gnielinski, Neue Gleichungen für den Wärme- und den Stoffübergang in turbulent durchströmten Rohren und Kanälen, Forsch. Im. Ingenieurwesen 41 (1) (1975) 8–16.